8-7-2020

Functional Morphology of Gliding Flight I. Modeling Reveals Distinct Performance Landscapes Based on Soaring Strategies

Lindsay D. Waldrop

Yanyan He

Tyson L. Hedrick

Jonathan Rader

Functional Morphology of Gliding Flight I. Modeling Reveals Distinct Performance Landscapes Based on Soaring Strategies

Functional morphology of gliding flight I. Modeling reveals distinct performance landscapes based on soaring strategies

Lindsay D. Waldrop
Schmid College of Science and Technology,
Chapman University, Orange, CA 92866 USA
Tel: +1 (714) 516-5615, Fax: +1 (714) 532-6048
waldrop@chapman.edu

Yanyan He
Depts. of Mathematics and Computer Science and Engineering,
University of North Texas, Denton, TX, USA
yanyan.he@unt.edu

Tyson L. Hedrick
Dept. of Biology,
University of North Carolina, Chapel Hill, NC, USA
thedrick@bio.unc.edu

Jonathan Rader
Dept. of Biology,
University of North Carolina, Chapel Hill, NC, USA
jrader@live.unc.edu

July 27, 2020

Abstract

The physics of flight influences the morphology of bird wings through natural selection on flight performance. The connection between wing morphology and performance is unclear due to the complex relationships between various parameters of flight. In order to better understand this connection, we present a holistic analysis of gliding flight that preserves complex relationships between parameters. We use a computational model of gliding flight, along with analysis by uncertainty quantification, to 1) create performance landscapes of gliding based on output metrics (maximum lift-to-drag ratio, minimum gliding angle, minimum sinking speed, lift coefficient at minimum sinking speed); and 2) predict what parameters of flight

(chordwise camber, wing aspect ratio, Reynolds number) would differ between gliding and non-gliding species of birds. We also examine performance based on soaring strategy for possible differences in morphology within gliding birds. Gliding birds likely have greater aspect ratios than non-gliding birds, due the high sensitivity of aspect ratio on most metrics of gliding performance. Furthermore, gliding birds can use two distinct soaring strategies based on performance landscapes. First, maximizing distance traveled (maximizing lift-to-drag ratio and minimizing gliding angle) should result in wings with high aspect ratios and middling-to-low wing chordwise camber. Second, maximizing lift extracted from updrafts should result in wings with middling aspect ratios and high wing chordwise camber. Following studies can test these hypotheses using morphological measurements.

Keywords: uncertainty quantification; bird; XFLR5; camber; aspect ratio; sensitivity analysis; generalized polynomial chaos

Running title: Modeling gliding flight in birds

List of Abbreviations

A – Output variance based on gPC surrogate
α – Angle of attack
α_{I} – Ideal angle of attack
AR – Aspect ratio of wing (eq. 2)
C – Chordwise camber of wing
$\overline{C}$ – Mean chordwise camber of wing
C_D – Coefficient of drag
CFD – Computational fluid dynamics
C_L – Coefficient of lift (eq. 4)
C_L/C_D – Lift-to-drag ratio
D – Drag force
Γ – Vortex strength times length of panel in model
γ – Glide angle
L – Lift force
L_{wz} – Projection of lift force in the direction vertical to wind
ν – Kinematic viscosity of air
Q – Wing chordwise camber
Q_{line} – Mean chordwise camber line of model wing
Re – Reynolds number (eq. 1)
ρ – Density of air
S – Plan area of wing (without body)
SI – Sobol index
$\vec{u}$ – gPC derived surrogate function
t – Wing chordwise maximum height
UQ – Uncertainty quantification
$u_p(\boldsymbol{\xi})$ – gPC surrogate function
V – Free-stream air speed
V_z – Sinking speed
$V_{z,\mathrm{min}}$ – Minimum sinking speed

VLM – Vortex lattice method
W – Wing length
x/c – Boundary layer transition point

1 Introduction

A key innovation in the history of life is the free flight of birds. As a result of this innovation, bird lineages have been hugely successful: there are over 10,000 extant species of birds with distributions spread all over the world (Altshuler et al., 2015). Along with occupying a large number of niches and habitats, birds possess a variety of wing morphologies and flight behaviors (Fig. 1).

Bird wings interact with air (and sometimes water) to enable locomotion. Since flight is a physical process, the shape and size of wings and their movements should impact flight performance, and in turn, differences in flight performance will influence the shape and size of wings through natural selection. Although birds are well studied as a group, the reasons behind differences in wing morphologies remain obscure (Taylor and Thomas, 2014; Baliga et al., 2019).

The flight apparatus in birds is a complex functional system with many parameters. Parameter variation often affects performance outputs of these systems in unexpected ways. Some input parameters are more mechanically sensitive to change than others, potentially affecting the distribution of morphological change (Muñoz, 2019). Additionally, different combinations of parameters can result in the same performance output (called "many-to-one mapping"), which is thought to be a fundamental driver of biodiversity in functional systems and a way to blunt the impact of changing sensitive features (Wainwright et al., 2005; Higham et al., 2016; Holzman et al., 2011; Muñoz, 2019).

In order to better understand the connection between flight physics and wing morphology, we present a simple computational model of gliding flight analyzed through uncertainty quantification (UQ). Modeling offers the ability to assess performance of the full parameter space available during evolution, including parameter combinations representing extant species, extinct and intermediate forms, as well as extremes not observed or perhaps even possible in nature (Koehl, 2003). UQ can create performance landscapes to holistically understand parameter effects and estimate the performance of individuals (Waldrop et al., 2018). Performance landscapes generated by computational models have been used as a way to assess evolution and biodiversity (e.g. Polly et al., 2016; Waldrop et al., 2018; Martinez and Wainwright, 2019; Stayton, 2019; Muñoz, 2019).

Birds support themselves in the air using either flapping or gliding flight. During non-gliding (flapping) flight, wings produce both lift (force that counteracts gravity, L) and thrust (force that produces forward motion). The wings and the body also produce drag (D), a force acting against forward motion. During gliding flight, outstretched wings produce only aerodynamic lift and drag, respectively perpendicular and parallel to the direction of airflow (Fig. 2). Forward motion is generated by loss of potential energy (altitude). Gliding can be characterized using the glide angle γ and sinking speed V_z, the vertical component of flight velocity (Fig. 2). These broadly describe the role of drag in reducing the altitude of birds in flight compared to the lift generated by their wings.

Many gliding birds take advantage of energy in the environment to counteract sinking due to drag, these behaviors are collectively called soaring. Compared to flapping flight,

soaring is energetically efficient since potential energy is derived from the environment (Cone, 1962). Birds use soaring to stay aloft for extended periods of time, making tasks such as foraging and long distance migration less energetically expensive (Hedenström, 1993; Pennycuick, 2002; Weimerskirch et al., 2003; Huey and Deutsch, 2016; Hedrick et al., 2018).

Soaring birds can use a variety of types of updrafts to stay aloft (Cone, 1962; Hedenström, 1993). Updrafts can be thermal (updrafts due to heating of the substratum), orographic (updrafts caused by physical structures deflecting wind, e.g. trees, buildings, cliffs), and dynamic (areas of high wind shear) (Katzner et al., 2015). Many birds use primarily thermals (falcons, vultures, frigate birds) and some use primarily dynamic soaring (albatross, storm petrels) (e.g. Pennycuick, 1998, 2002; Akos et al., 2008; Huey and Deutsch, 2016). Most soaring birds likely use a mixture of updraft types depending on the features of the location, updraft availability, and purpose (Katzner et al., 2015; Mallon et al., 2016).

Gliding and soaring performance can be assessed using many different strategies. For our work, we focus on two strategies: maximizing the distance traveled or minimizing the sinking speed, which maximizes energy extracted from updrafts. Distance traveled is maximized at the minimum of glide angle (γ), the cotangent of the lift-to-drag ratio. Thus, increasing the maximum lift-to-drag ratio increases the distance traveled. Alternatively, birds could also maximize the energy extracted from updrafts by minimizing sinking speed (V_z), typically at a slightly slower flight speed and with higher lift coefficient than that where lift-to-drag is maximized. Although similar, both strategies are distinct enough to potentially place differing selective pressures on wing morphology.

In this study and the following companion work (Rader et al., 2020), we used a model of gliding flight and morphological data collected via 3D scanning of museum bird spread-wing collections to address the following questions:

1. Can we pinpoint the parameters, or combination of parameters, of wings that lead to differential performance between gliding/soaring and non-gliding birds?

2. Among birds that glide, do the performance landscapes suggest distinct morphologies for an '"aerial perch"' flight strategy where the bird remains aloft but does not change location versus an "aerial search" strategy of using soaring to move about the landscape?

To address these questions, we used XFLR5 (Deperrois, 2010) to model a gliding bird and vary three parameters: aspect ratio, wing chordwise camber, and Reynolds number. We varied these parameters based on measurements from a wide variety of extant species (see Rader et al., 2020). Using uncertainty quantification, we constructed a surrogate function to create predictive landscapes of different performance outputs (maximum lift-to-drag ratio, minimum sinking speed, lift coefficient at minimum sinking speed, and ideal angle of attack) that could be influenced by selection to shape wing morphology. The morphological parameters under consideration here have been investigated before and their individual effects on wing performance are generally known. However, our methods allow for simultaneous consideration of multiple effects and their potential interactions to produce a multi-dimensional performance landscape relevant to known variation in bird wing morphology.

2 Materials and Methods

2.1 Modeling of low-Reynolds number gliding wings

2.1.1 XFOIL and XFLR5

For this study, we used XFLR5 (version 6.47), an implementation of XFOIL and the ring vortex lattice method (VLM) in C++ (Deperrois, 2010). XFLR5 is a user-friendly program created for the design and analysis of model aircraft, based on low-Reynolds number aerodynamics appropriate for studying the gliding flight of birds. XFLR5 has been experimentally validated comparing lift, drag, and pressure coefficients at *Re* and angles of attack relevant to birds, see Supplemental Information for additional discussion (e.g. Communier et al., 2015; Güzelbey et al., 2018).

XFLR5 relies on XFOIL code for generating two-dimensional polars for airfoils. XFOIL estimates flow around 2D airfoils using a potential flow panel method with fully coupled inviscid and viscous solvers (Drela, 1989). XFOIL is a popular and accessible technique for estimating flow around airfoils (e.g. Marten et al., 2010; Lafountain et al., 2012; De Tavernier et al., 2018), and it gives comparable prediction results with low computational costs as compared to full CFD modeling techniques (Morgado et al., 2016).

XFLR5 extends the 2D polars produced by XFOIL into three dimensions using the ring vortex lattice method (VLM) based on a wing shape defined by the user (Fig. 3A & B). The wing is divided into panels and VLM produces a ring vortex associated with each panel (Fig. 3A, between numbered lines); and VLM uses only the mean camber line (Q_{line}) in place of the chordwise camber of the wing (see Fig. 2 bottom). The force produced by the vortex on each panel is summed to calculate the total lift and the lift coefficient (equations 3 & 4, Fig. 3C). This method is linear and inviscid, although using the 2D polars from XFOIL provides input for viscous effects. VLM is appropriate for thin surfaces, small angles of attack (see Fig. 2 bottom), and a range of wing aspect ratios (including low aspect ratios) (Deperrois, 2010). We employed the modified version of the classic VLM (VLM2 option in XFLR5) based on (Katz and Plotkin, 2001) where only trailing vortices extend to infinity, representing the wake of the wing.

For all models, Neumann boundary conditions were used for VLM calculations. The density of air in the model was $\rho = 1.225$ kg m^{-3} and the kinematic viscosity was $\nu = 1.5 \times 10^{-5}$ m^2 s^{-1}. Boundary layer transition points were set to 0.05 x/c for the top and bottom of the airfoil. Body panels were ignored for all analyses.

The Reynolds number of the model was varied. Reynolds number was based on mean chord length $\overline{C}$:

$$Re = \frac{V\overline{C}}{\nu}. \quad (1)$$

In this study, $\overline{C}$ and ν were held constant, so to achieve a range of *Re* from 10,000 to 200,000, the free-stream air speed V was varied from 1.5 to 30 m s^{-1}.

2.1.2 Wing geometry and airfoil design

For the model in the present work, we drew our measured values for each input parameter from Rader et al. (2020). Briefly, the sample includes 127 species from 22 lineages of songbirds, shorebirds, seabirds, and raptors, and approximates the ranges of parameter values for extant birds. The ranges of input parameters for our model were expanded by at least 5 percent beyond the upper and lower bounds for each parameter in the sample

of wings.

In order to create the initial airfoil for the bird model, we used a published airfoil cross section based on the wing of a wandering albatross to serve as a template (Ananda and Selig, 2018). This airfoil template was then rescaled to change wing maximum height t to produce different values of Q, where wing chordwise camber Q is defined as $Q = t/C$. Wing chord C was kept constant. Values of Q varied between 0 and 0.2. (Note that $Q = 0$ implies zero wing maximum height. Since only the mean camber line, Q_{line}, of the wing was used for calculations, varying maximum height in this way does not affect calculations.) Wing chord varied along the wing at each numbered section indicated in Fig. 3A, proportions of which were based on the aggregate observations of the plan areas of 41 species of songbirds (Passeriformes) and raptors (Falconiformes). For a list of these taxa, see the Supplemental Information. The mean chord of sections 1 through 6 was held constant at $\overline{C} = 0.100$ m. There was no twist in any model wings.

The model's aspect ratio was also varied. Aspect ratio (AR) of the bird model is defined, following Ellington (1984), as:

$$AR = \frac{(2W)^2}{S}, \tag{2}$$

where W is the length of one wing and S is plan area of both wings combined (see Fig. 3A). In order to vary AR, the wing's $\overline{C}$ was held constant at 0.100 m and the length of the wing was varied between 0.166 to 0.664 m to yield values of AR from 3.00 to 12.0. Note that increasing AR in this way also increases S. Furthermore, because our wing span and area terms for AR do not include the body, the reported AR is slightly less than in studies where span is defined as wing tip to wing tip and wing area includes the area of the body.

In order to examine the effects of wing loading on minimum sinking speed $V_{z,\min}$, two conditions were created. First, the model was given a constant mass of 0.9 kg, which caused wing loading to vary as the area of the wing changed with changing AR. Second, the mass of the bird was varied such that the wing loading of the model was kept constant at 7.5 kg m^{-2}. Note that all output values rely on the constant mass case except $V_{z,\min}$ where specifically noted as constant wing loading.

2.1.3 Analysis of Results

Within XFLR5, both lift and induced drag forces are calculated using the far-field method (Trefftz Plane) (Deperrois, 2010). The lift force L is calculated as the force acting normal to each panel of the wing:

$$L = \rho V \times \Gamma \tag{3}$$

where Γ is the vortex strength times its length. The lift coefficient C_L is defined as:

$$C_L = \frac{1}{\rho S V^2} \sum_{\text{panels}} L_{wz} \tag{4}$$

where L_{wz} is the projection of the lift force on the axis vertical to the direction of wind. The force of induced drag is calculated similar to eq. 3 except using the force of each panel opposite the direction of flow. Similarly to C_L (eq. 4), the forces imparted to each panel are then summed and divided by $\rho S V^2$ to obtain the induced drag coefficient. Viscous drag is estimated by interpolation of the XFOIL polars. Total drag used to estimate the

drag coefficient (C_D) includes both induced and viscous components (for information on drag calculations, see Drela and Giles, 1987; Drela, 1989).

For each Q, AR, and Reynolds number parameter combination, angles of attack (Fig. 2 bottom) were varied between -5° and 7°. In order to determine the ideal angle of attack α_{I} and maximum lift-to-drag (C_L/C_D) ratios, values of C_L/C_D were plotted against angles of attack α (Fig. 3E). The curve of C_L/C_D vs. α was reconstructed with a smooth-spline fit and the maximum C_L/C_D value was found on this fit curve. The corresponding α at max C_L/C_D was recorded as α_{I} (Fig. 3E labeled on graph for $V = 10.9$).

A similar process as described above for maximum C_L/C_D was used to recover minimum sinking speed ($V_{z,\mathrm{min}}$). Sinking speed was plotted against α (similar to Fig. 3E). The subsequent curve was reconstructed with a smooth-spline fit and the minimum output value, $V_{z,\mathrm{min}}$, was recorded. The corresponding angle of attack and lift coefficient were recorded as $\alpha_{z,\mathrm{min}}$ and C_L at $V_{z,\mathrm{min}}$.

The relationship between α and C_L was further examined by fitting a linear model to the values recorded for each airfoil. The resulting slope and intercept for the relationship were then recorded. Additional discussion on these analysis methods can be found in the Supplemental Information.

2.2 Uncertainty quantification

2.2.1 Generalized Polynomial Chaos Expansion

Generalized polynomial chaos (gPC) expansion method is an important uncertainty quantification technique for studying the uncertainty in the simulation of a physical system, and consequently helping to provide more reliable and meaningful analyses for the system behavior. Specifically, it constructs a way to estimate a full model by creating a computationally cheaper surrogate function over the stochastic space. This surrogate function can then be used to approximate the full simulation so that the uncertainty in the model output can be represented more efficiently.

Compared to the traditionally used Monte Carlo (MC) method, which is intuitive and easy to implement, the gPC method requires a far smaller number of samples to reach the same accuracy for low-dimensional problems, and hence its efficiency can be orders of magnitude higher (Xiu et al., 2003; Xiu and Karniadakis, 2003). While Monte Carlo method normally needs ten thousand or more number of realizations to conduct an accurate uncertainty analysis, the gPC method can accomplish the same task with hundreds or fewer simulations. The adoption of an efficient gPC method can improve our ability to study complex CFD models.

In order to model a full simulation (in this work, the XFLR5 model of a gliding bird), gPC method first uses uncorrelated input parameters selected by the user. The gPC expansion uses probability distribution functions of each input parameter within a defined range to construct a set of full simulations. The output values of this select set of simulations forms the basis of constructing the surrogate function used.

In this study, we chose three parameters that are known to impact gliding performance in birds: aspect ratio (AR), wing chordwise camber (Q), and Reynolds number (Re). We varied the parameters of interest over a range and distribution reflective of extant birds. Aspect ratio (AR, eq. 2) varied from 3.0 to 12.0, wing camber Q varied from 0.0 to 0.2, and Reynolds number (Re, eq. 1) varied from 10,000 to 200,000. Because densely sampling this parameter space is computationally infeasible, even with XFLR5, the influence of different parameter combinations was quantified via UQ on the output

performance metrics (maximum C_L/C_D, ideal angle of attack α_I, minimum sinking speed $V_{z,/textmin}$, and coefficient of lift at minimum sinking speed C_L at $V_{z,/textmin}$).

From this set of input parameters and distributions, we sample the input space to create a set of full simulations to run with the XFLR5 model. Then, the gPC expansion method is applied to approximate the full model (or the true model output) $u(\boldsymbol{\xi})$ with a cheaper surrogate model $u_p(\boldsymbol{\xi})$. We provide the basics of gPC expansion in the Supplemental Information.

The gPC expansion is constructed based on a set of 681 simulations that varied in AR, Q, and Re that were run through the full XFLR5 model. This simulation set ranged from $AR = [3.229, 11.771]$, $Q = [0.005089, 0.194911]$, and $Re = [14835, 195165]$ (Fig. 3F). After running these simulations, we obtained the results below which are reported in terms of the "raw simulation data", or the output values from the set of full simulations, and the "surrogate function" ($u_p(\boldsymbol{\xi})$) values calculated across the full range of input parameter values (Fig. 3G). The range from surrogate functions produced through uncertainty quantification slightly differs from the range of full simulations because: (1) the continuous parameter space of the surrogate versus the discrete samples of full simulation data, and (2) the approximation in surrogate construction versus the exact simulation. The surrogate functions $u_p(\boldsymbol{\xi})$ for each output performance value served as our theoretical performance landscapes of gliding flight (i.e. Figs. 3G, 4, 5, & 6).

2.2.2 Sensitivity Analysis

Based on the gPC expansion, one can efficiently calculate a variance-based measure – Sobol indices (SI), which measure the global sensitivity of quantity of interest with respect to the uncertainty in random input parameters over the whole stochastic space (Sudret, 2008). Under the assumption of mutually independent random variables, the calculation is conducted using analysis of variance (ANOVA) decomposition, and defined as the ratio of the variance in sub-dimensional problem to the total variance of the full-dimensional problem (Sobol, 1993, 2001; Sudret, 2008). It can be calculated even when the model is non-linear and non-monotonic. The higher SI ratio indicates more importance of the set of input parameters in that sub-dimensional space. We calculated SI's based on the gPC expansion, additional details are given in the Supplemental Information.

The Sobol indices of the quantity of interest with respect to all individual or combination of the input parameters sum to the unity, i.e. one. The uncertainty in the individual or combination of input parameters with the higher Sobol indices have more impact on the quantity of interest. Therefore, we can rank the importance of the uncertain variables by comparing the Sobol indices and focus on the exploration of those important variables in the physical process. Note: Sobol indices measure the global sensitivity with the consideration of the whole variation range of the inputs, which is pre-specified based on experts' opinion or the collected data from literature. An accurate rank of the input parameters is obtained under the assumption of accurate estimation of the whole variation range.

2.3 Data Availability

All code, XFLR5 files, and results available at:
https://github.com/lindsaywaldrop/birdwingGPC.

3 Results

3.1 Effects on lift-to-drag ratio and minimum glide angle

Maximum lift-to-drag ratio, max C_L/C_D, values for the raw simulation data range from 4.59 to 21.1. Max C_L/C_D values for the surrogate function range from 3.46 to 20.8, due to the parameter space of the surrogate slightly extending beyond the range of the simulations (Fig. 4 left column). These max C_L/C_D values are broadly consistent with measured values on birds and individual wings under experimental and field conditions (Pennycuick, 1960, 1968; Parrot, 1970; Tucker and Parrott, 1970; Withers, 1981; Tucker and Heine, 1990; Tucker, 1991; Rosen and Hedenström, 2001; Henningsson and Hedenström, 2011). Values of minimum glide angle, min γ, ranged between 2.71° to 12.3° in the raw simulation data and 2.22° and 15.6° for the surrogate function; these numbers are also consistent with published observations of glide angles for birds (Pennycuick, 1971; Tucker and Heine, 1990; Spaar, 1997). For more detailed comparisons of the XFLR5 model against literature values of flight, see the Supplemental Information.

The lowest values of max C_L/C_D occur at high Q and low AR, and the highest values occur at intermediate to low Q and high AR. Reflecting the surrogate values, the Sobol indices indicate that max C_L/C_D is sensitive to changes in both AR and Q (Table 1). Max C_L/C_D is broadly insensitive to changes in Re and parameter interactions (Table 1; Fig. 4 bottom left).

3.2 Effects on minimum sinking speed

Minimum sinking speeds ($V_{z,\min}$) extracted from the model show a range of values from 0.602 to 4.56 m s^{-1} for the constant mass case and 0.658 to 2.69 m s^{-1} for the constant wing-loading case. The range for the surrogate function was 0.273 to 5.72 m s^{-1} for the constant mass case and 0.454 to 3.35 m s^{-1} for the constant wing-loading case. Note that Fig. 5 shows that variation in performance in both cases is largely due to AR and Q, and follows the same overall pattern.

For $V_{z,\min}$, low values of AR lead to poor performance and high AR leads to the lowest values of $V_{z,\min}$ (Fig. 5). This is reflected in the Sobol indices: $V_{z,\min}$ is primarily controlled by AR. Q has a much smaller effect, and $V_{z,\min}$ is insensitive to other parameters and their interactions (Table 1).

Calculated values of lift coefficient at minimum sinking speed, C_L at $V_{z,\min}$, for the raw simulation data ranged from 0.273 to 1.39 and the surrogate function values ranged from 0.186 to 1.40 (Fig. 4 right). These values are consistent with published lift coefficients (Pennycuick, 1960, 1968, 1971, 1983; Withers, 1981; Tucker and Heine, 1990; Rosen and Hedenström, 2001; Henningsson and Hedenström, 2011, see also Supplemental Information). Sensitivities of C_L at $V_{z,\min}$ show that Q exerts the most influence, followed by AR. Other parameters and interactions were not influential (Table 1). The highest values for C_L at $V_{z,\min}$ (highest performance) occur with high values of Q and high values of AR.

3.3 Effects on ideal angle of attack

The ideal angle of attack α_{I} represents the α where C_L/C_D exhibits its maximum value. α_{I} varied in the raw simulations from -3.10° to 4.05° and in the surrogate function from -4.63° to 4.54° (Fig. 6). Values of α_{I} are very sensitive to changes in Q, somewhat sensitive to AR, and insensitive to changes in Re (Fig. 6; Table 1). Increasing AR or Q increases

the frontal area of the wing that is exposed to flow, with a corresponding increase in drag. This interacts positively with α, and as a result, the highest values of C_L/C_D are found closer to $\alpha = 0$. $\alpha_{\mathrm{I}} = 0$ is noted on Fig. 6 center as a black line.

Ideal angle of attack α_{I} was insensitive to most interactions, but two notable exceptions are Q and Re (Table 1), giving the total $SI(Re) > 0.10$. These SI's indicate that while Re does not directly influence variability on α_{I}, it has effects through interactions with the other parameters.

The slope and y-intercept surrogates and sensitivities break down the pattern of C_L at $V_{z,\min}$. The slope of this line represents the gain of C_L at $V_{z,\min}$ per degree of α, and values ranged between 0.0330 unit per degree and 0.0787 unit per degree for the raw simulations and 0.0301 unit per degree and 0.0797 unit per degree for the surrogate function. The slope's sensitivity is entirely controlled by changes in AR and insensitive to all other parameters and interactions (Table 1). In contrast, the y-intercept, which represents the value of C_L at $V_{z,\min}$ at $\alpha = 0°$, is most sensitive to Q and somewhat sensitive to AR, with all other parameters and interactions have SI's < 0.03 (Table 1). Y-intercepts range from 0.1235 to 1.2788 in the raw data and 0.0557 to 1.3677 for the surrogate function.

4 Discussion

Birds use flight in a huge variety of habitats and niches that is reflected in the diversity of their wing morphology. Flight performance relies on the physics of flight, and flight represents a complex functional system that is difficult to understand by examining system components in a piecemeal fashion. To form a more holistic understanding of how aspects of wing morphology and kinematics influence flight performance, we created a simple model of gliding flight and sampled a complete parameter space over biologically relevant ranges of aspect ratio (AR), chordwise camber (Q), and Reynolds number (Re) using uncertainty quantification. This analysis created both surrogate functions of flight performance and sensitivity indices of each parameter and their interactions to better understand how morphology influences flight performance.

Our analysis on the model found that maximum lift-to-drag ratio (max C_L/C_D) was sensitive to changes in both aspect ratio and chordwise camber, attaining maximum values at lower values of camber and very high values of aspect ratio (Fig. 4 left). Minimum glide angle (min γ) followed these patterns in sensitivity and high performance combinations of aspect ratio and camber. Gliding performance in terms of maximizing the horizontal distance traveled relative to altitude lost relies heavily on having a large aspect ratio and relatively low camber wings. These results are consistent with biological data, including Taylor and Thomas (2014)'s phylogenetically corrected analysis which found that aspect ratio and wing area are correlated with exclusively pelagic soaring and soaring over land (also see Pennycuick, 1971; Tucker, 1987). Conventional airfoil analysis also typically highlights the importance of aspect ratio and camber in determining max C_L/C_D, (e.g. Tietjens, 1957).

Minimum sinking speed ($V_{z,\min}$) was most sensitive to changes in aspect ratio and broadly insensitive to other parameters, including camber (Fig. 5). Furthermore, unlike max C_L/C_D, $V_{z,\min}$ exhibits little further performance improvement for aspect ratios greater than ≈ 7. Thus, thermal soaring or an "aerial perch" type foraging strategy, where the bird seeks to survey a large area from above but not necessarily move about

the landscape, is accessible to a much wider range of wing parameter space than an "aerial search" strategy that requires forward motion.

Similar to the maximum lift-to-drag ratio and minimum sinking speed, high values of lift coefficient at minimum sinking speed (C_L at $V_{z,\min}$) rely on moderate-to-high aspect ratio, and in contrast to $V_{z,\min}$, high values of C_L at $V_{z,\min}$ rely also on large values of chordwise camber (Fig. 4 right). High values of lift by highly cambered wings are evidenced by the higher y-intercept values (or lift at zero angle of attack), consistent with other analyses including those on bat wings and insect wings (Stockwell, 2001; Young et al., 2009; Zheng et al., 2013) as well as conventional airfoils (Winslow et al., 2018). Higher lift comes at the expense of increased drag on highly cambered wings, which have a larger frontal area than less cambered wings.

Insensitivity to Reynolds number (Re), in this study a metric of flight speed and wing size, suggests that broad ranges of flight speed and body size do not affect measures of overall flight performance (e.g. max C_L/C_D, C_L at $V_{z,\min}$). The ideal angle of attack (α_I) of the wing was somewhat sensitive to parameter interactions involving Reynolds number, suggesting that operating angles may be actively controlled by birds depending on their flight speeds in order to offset small changes in flight performance.

Based on these results, we offer the following hypotheses to answer our original questions:

1. Gliding and non-gliding birds will have different combinations of aspect ratios and chordwise camber. High-performance gliders will likely exhibit large wings with high aspect ratios as compared to non-gliding birds.

2. Gliding and soaring birds have two potential strategies: maximizing lift-to-drag ratio and minimizing sinking speed. These outputs each come with unique performance landscapes which indicate the potential for significant selection pressures based on flight performance. Specifically, they are:

    2a. Maximizing lift-to-drag ratio (Fig. 4 left), also minimizing glide angle, will have high aspect ratios and moderate to low chordwise camber in wings.

    2b. Minimizing sinking speed (Fig. 5) will drive moderate to high aspect ratios but not affect camber. Maximizing lift (Fig. 4 right) while minimizing sinking speed (Fig. 5), potentially an important trait for takeoff and load lifting performance in larger birds, will also drive high chordwise camber.

There is likely an effect of foraging style that separates the two gliding strategies (2a and 2b), similar to those suggested by other studies (Taylor and Thomas, 2014). Griffon vultures, in one study, were tracked for an average of 77 km per daily foraging bout (Monsarrat et al., 2013), contrasting with 1284 km average range for wandering albatrosses (Weimerskirch et al., 1993). These two birds exemplify the "aerial perch" versus "aerial search" flight strategies, respectively, which likely arise from differences in resource density or distribution between terrestrial and pelagic habitats. Species that operate in habitats with high density of foraging and predictable updrafts may be under selective pressure to minimize sinking speed to best exploit environmental sources of lift. By contrast, species that must search greater distances for food and with less effective sources of environmentally derived lift may be drawn toward a strategy of dynamic soaring, maximizing lift-to-drag ratio to increase distance travelled.

These hypotheses represent testable predictions on the role of flight physics in shaping the morphology of specialized bird wings. Although the model itself is a simplification of the complex process of flight, the model and our analysis is able to incorporate many sophisticated aspects of gliding flight while preserving the non-linear relationships inherent to the physics of flight. In the following study, Rader et al. (2020) uses a collection of 3D scanned bird wings 127 species representing 22 lineages of birds to test the hypotheses proposed herein. Our sample includes gliding taxa from all major lineages of North American raptors (e.g., hawks, falcons, and new-world vultures), several groups of seabirds (e.g., terns, petrels, and shearwaters), and shorebirds (e.g., phalaropes and woodcocks). We also included 12 lineages of songbirds, which tend not to glide, for comparison with the gliding taxa.

In this study, we chose three parameters thought to influence performance (Reynolds number, wing chordwise camber, and wing aspect ratio) while neglecting many others. This choice was in part because these parameters captured the major features of wing morphology while keeping the computational costs down. Parameters such as wing-tip shape, wing area, spanwise camber, and wing offset could all be included in this model in future studies.

As with all models, there are limitations inherent in the methodology and the assumptions that we've chosen for this study. We assume that birds will operate at optimal angles of attack to maximize C_L/C_D and minimize V_z, although this behavior is unknown. The vortex ring method is an inviscid solution to flight, with viscous effects being only incorporated indirectly through XFOIL. Since viscous effects are still important at the lower end of our Reynolds number range, this will likely underestimate the drag on the wings, leading to artificially high values of C_L/C_D. Furthermore, lift calculations such as these are sensitive to wake dynamics and produce inconsistent results (Gutierrez et al., 2016). In addition, there are several second-order effects that likely play a role in lift and drag that are not accounted for in our model: lift and drag produced by the body and tail of the bird (e.g. Henningsson et al., 2014; Usherwood et al., 2020); the role of wing flexibility and reconfiguration during flight (e.g. Platzer et al., 2008; Gopalakrishnan and Tafti, 2010); and slots created by wing-tip feathers (e.g. Baldwin et al., 2010; Grilli et al., 2017); among others.

Bird flight is a complex, multi-variable system of locomotion, and our model of the bird wing as an ideal airfoil represents a simplification of this system. Our model is neither the most detailed treatment nor the most general model that has been used to describe bird flight; past studies have ranged from linear correlations between variables to highly detailed computational fluid dynamics models (e.g. Hedenström, 1993; Yi et al., 2010; Taylor and Thomas, 2014; Taylor et al., 2016; Hassanalian et al., 2017; Ananda and Selig, 2018; Throneberry et al., 2019). This model is a balance between preserving the major, non-linear components of gliding flight and the computational demands of fluid modeling. By balancing these demands and using techniques that reduce the number of required simulations, we are able to create a problem that was both tractable (in terms of computational time and resources needed to complete it) and detailed enough to provide a unified, multi-parameter view of the first-order effects of wing morphology on gliding. Our conclusions on the effect of different morphological parameters on flight performance are broadly consistent with more computationally expensive or experimentally sophisticated studies, indicating that our combination of simpler computational models and gPC interpolation of parameter space performed adequately and should be a useful tool for future studies.

Acknowledgements

The authors would like to acknowledge the Society for Integrative and Biology for hosting the symposium "Melding Modeling and Morphology" out of which this work arose; the Company of Biologists for a small grant that supported travel for authors participating in our complementary sessions.

The authors wish to thank: Mostafa Hussenalian for helpful discussions regarding XFOIL and XFLR5; Sina Mohammadi for assistance with the computational model; Sarah Hester, Emilie Sandfeld, Lindsay Zumwalt, and two anonymous reviewers for assistance with the manuscript.

References

Akos, Z., Nagy, M., and Vicsek, T. (2008). Comparing bird and human soaring strategies. *Proceedings of the National Academy of Sciences*, 105(11):4139–4143.

Altshuler, D. L., Bahlman, J. W., Dakin, R., Gaede, A. H., Goller, B., Lentink, D., Segre, P. S., and Skandalis, D. A. (2015). The biophysics of bird flight: functional relationships integrate aerodynamics, morphology, kinematics, muscles, and sensors. *Canadian Journal of Zoology*, 93(12):961–975.

Ananda, G. K. and Selig, M. S. (2018). Design of bird-like airfoils. In *2018 AIAA Aerospace Sciences Meeting*, page 0310.

Baldwin, M. W., Winkler, H., Organ, C., and Helm, B. (2010). Wing pointedness associated with migratory distance in common-garden and comparative studies of stonechats (*Saxicola torquata*). *Journal of Evolutionary Biology*, 23(5):1050–1063.

Baliga, V., Szabo, I., and Altshuler, D. (2019). Range of motion in the avian wing is strongly associated with flight behavior and body mass. *Science Advances*, 5(10):eaaw6670.

Communier, D., Salinas, M. F., Carranza Moyao, O., and Botez, R. M. (2015). Aero structural modeling of a wing using CATIA V5 and XFLR5 software and experimental validation using the Price-Païdoussis wing tunnel. In *AIAA atmospheric flight mechanics conference*, page 2558.

Cone, C. D. (1962). The soaring flight of birds. *Scientific American*, 206(4):130–142.

De Tavernier, D., Baldacchino, D., and Ferreira, C. (2018). An integral boundary layer engineering model for vortex generators implemented in XFOIL. *Wind Energy*, 21(10):906–921.

Deperrois, A. (2010). XFLR5 – analysis of foil sand wings operating at low Reynolds numbers. http://xflr5.sourceforge.net/xflr5.htm.

Drela, M. (1989). XFOIL: An analysis and design system for low Reynolds number airfoils. In *Low Reynolds Number Aerodynamics*, pages 1–12. Springer.

Drela, M. and Giles, M. B. (1987). Viscous-inviscid analysis of transonic and low Reynolds number airfoils. *AIAA journal*, 25(10):1347–1355.

Ellington, C. P. (1984). The aerodynamics of hovering insect flight. II. Morphological parameters. *Philosophical Transactions of the Royal Society of London. B, Biological Sciences*, 305(1122):17–40.

Gopalakrishnan, P. and Tafti, D. K. (2010). Effect of wing flexibility on lift and thrust production in flapping flight. *AIAA journal*, 48(5):865–877.

Grilli, M. G., Lambertucci, S. A., Therrien, J.-F., and Bildstein, K. L. (2017). Wing size but not wing shape is related to migratory behavior in a soaring bird. *Journal of Avian Biology*, 48(5):669–678.

Gutierrez, E., Quinn, D. B., Chin, D. D., and Lentink, D. (2016). Lift calculations based on accepted wake models for animal flight are inconsistent and sensitive to vortex dynamics. *Bioinspiration & Biomimetics*, 12(1):016004.

Güzelbey, İ. H., Eraslan, Y., and Doğru, M. H. (2018). Numerical investigation of different airfoils at low Reynolds number in terms of aerodynamic performance of sailplanes by using XFLR5. *Karadeniz Fen Bilimleri Dergisi*, 8(1):47–65.

Hassanalian, M., Abdelkefi, A., Wei, M., and Ziaei-Rad, S. (2017). A novel methodology for wing sizing of bio-inspired flapping wing micro air vehicles: theory and prototype. *Acta Mechanica*, 228(3):1097–1113.

Hedenström, A. (1993). Migration by soaring or flapping flight in birds: the relative importance of energy cost and speed. *Philosophical Transactions of the Royal Society of London. Series B: Biological Sciences*, 342(1302):353–361.

Hedrick, T. L., Pichot, C., and De Margerie, E. (2018). Gliding for a free lunch: biomechanics of foraging flight in common swifts (*Apus apus*). *Journal of Experimental Biology*, 221(22):jeb186270.

Henningsson, P. and Hedenström, A. (2011). Aerodynamics of gliding flight in common swifts. *Journal of Experimental Biology*, 214(3):382–393.

Henningsson, P., Hedenström, A., and Bomphrey, R. J. (2014). Efficiency of lift production in flapping and gliding flight of swifts. *PloS One*, 9(2):e90170.

Higham, T. E., Rogers, S. M., Langerhans, R. B., Jamniczky, H. A., Lauder, G. V., Stewart, W. J., Martin, C. H., and Reznick, D. N. (2016). Speciation through the lens of biomechanics: locomotion, prey capture and reproductive isolation. *Proceedings of the Royal Society B: Biological Sciences*, 283(1838):20161294.

Holzman, R., Collar, D. C., Mehta, R. S., and Wainwright, P. C. (2011). Functional complexity can mitigate performance trade-offs. *The American Naturalist*, 177(3):E69–E83.

Huey, R. B. and Deutsch, C. (2016). How frigate birds soar around the doldrums. *Science*, 353(6294):26–27.

Katz, J. and Plotkin, A. (2001). *Low-speed aerodynamics*, volume 13. Cambridge University Press.

Katzner, T. E., Turk, P. J., Duerr, A. E., Miller, T. A., Lanzone, M. J., Cooper, J. L., Brandes, D., Tremblay, J. A., and Lemaître, J. (2015). Use of multiple modes of flight subsidy by a soaring terrestrial bird, the golden eagle *Aquila chrysaetos*, when on migration. *Journal of the Royal Society Interface*, 12(112):20150530.

Koehl, M. (2003). Physical modeling in biomechanics. *Philos. T. Roy. Soc. B*, 358:1589–1596.

Lafountain, C., Cohen, K., and Abdallah, S. (2012). Use of XFOIL in design of camber-controlled morphing UAVs. *Computer Applications in Engineering Education*, 20(4):673–680.

Mallon, J. M., Bildstein, K. L., and Katzner, T. E. (2016). In-flight turbulence benefits soaring birds. *The Auk: Ornithological Advances*, 133(1):79–85.

Marten, D., Pechlivanoglou, G., Nayeri, C., and Paschereit, C. (2010). Integration of a WT blade design tool in XFOIL/XFLR5. In *10th German Wind Energy Conference (DEWEK 2010), Bremen, Germany, Nov*, pages 17–18.

Martinez, C. M. and Wainwright, P. C. (2019). Extending the geometric approach for studying biomechanical motions. *Integrative and Comparative Biology*, 59(3):684–695.

Monsarrat, S., Benhamou, S., Sarrazin, F., Bessa-Gomes, C., Bouten, W., and Duriez, O. (2013). How predictability of feeding patches affects home range and foraging habitat selection in avian social scavengers? *PloS One*, 8(1).

Morgado, J., Vizinho, R., Silvestre, M., and Páscoa, J. (2016). XFOIL vs CFD performance predictions for high lift low Reynolds number airfoils. *Aerospace Science and Technology*, 52:207–214.

Muñoz, M. M. (2019). The evolutionary dynamics of mechanically complex systems. *Integrative and Comparative Biology*, 59(3):705–715.

Parrot, G. (1970). Aerodynamics of gliding flight of a black vulture *Coragyps atratus*. *Journal of Experimental Biology*, 53(2):363–374.

Pennycuick, C. (1960). Gliding flight of the fulmar petrel. *Journal of Experimental Biology*, 37(2):330–338.

Pennycuick, C. (1998). Field observations of thermals and thermal streets, and the theory of cross-country soaring flight. *Journal of Avian Biology*, pages 33–43.

Pennycuick, C. J. (1968). A wind-tunnel study of gliding flight in the pigeon *Columba livia*. *Journal of Experimental Biology*, 49(3):509–526.

Pennycuick, C. J. (1971). Gliding flight of the white-backed vulture *Gyps africanus*. *Journal of Experimental Biology*, 55(1):13–38.

Pennycuick, C. J. (1983). Thermal soaring compared in three dissimilar tropical bird species, *Fregata magnificens*, *Pelecanus occidentals* and *Coragyps atratus*. *Journal of Experimental Biology*, 102(1):307–325.

Pennycuick, C. J. (2002). Gust soaring as a basis for the flight of petrels and albatrosses (Procellariiformes). *Avian Science*, 2(1):1–12.

Platzer, M. F., Jones, K. D., Young, J., and Lai, J. C. (2008). Flapping wing aerodynamics: progress and challenges. *AIAA Journal*, 46(9):2136–2149.

Polly, P. D., Stayton, C. T., Dumont, E. R., Pierce, S. E., Rayfield, E. J., and Angielczyk, K. D. (2016). Combining geometric morphometrics and finite element analysis with evolutionary modeling: towards a synthesis. *Journal of Vertebrate Paleontology*, 36(4):e1111225.

Rader, J., He, Y., Hedrick, T., and Waldrop, L. (2020). Functional morphology of gliding flight II. Morphology follows predictions of gliding performance. *Integrative and Comparative Biology*, submitted.

Rosen, M. and Hedenström, A. (2001). Gliding flight in a jackdaw: a wind tunnel study. *Journal of Experimental Biology*, 204(6):1153–1166.

Sobol, I. M. (1993). Sensitivity estimates for nonlinear mathematical models. *Mathematical Modeling and Computational Experiments*, 1:407–414.

Sobol, I. M. (2001). Global sensitivity indices for nonlinear mathematical models and their Monte Carlo estimates. *Mathematics and Computers in Simulation*, 55:271–280.

Spaar, R. (1997). Flight strategies of migrating raptors; a comparative study of interspecific variation in flight characteristics. *Ibis*, 139(3):523–535.

Stayton, C. T. (2019). Performance surface analysis identifies consistent functional patterns across 10 morphologically divergent terrestrial turtle lineages. *Integrative and Comparative Biology*, 59(2):346–357.

Stockwell, E. F. (2001). Morphology and flight manoeuvrability in New World leaf-nosed bats (Chiroptera: Phyllostomidae). *Journal of Zoology*, 254(4):505–514.

Sudret, B. (2008). Global sensitivity analysis using polynomial chaos expansions. *Reliability Engineering & System Safety*, 93(7):964–979.

Taylor, G. K., Reynolds, K. V., and Thomas, A. L. (2016). Soaring energetics and glide performance in a moving atmosphere. *Philosophical Transactions of the Royal Society B: Biological Sciences*, 371(1704):20150398.

Taylor, G. K. and Thomas, A. L. (2014). *Evolutionary biomechanics: selection, phylogeny, and constraint*. Oxford University Press (UK).

Throneberry, G., Hassanalian, M., and Abdelkefi, A. (2019). Insights into sensitivity of wing shape and kinematic parameters relative to aerodynamic performance of flapping wing nano air vehicles. *Drones*, 3(2):49.

Tietjens, O. (1957). *Applied hydro- and aeromechanics: based on lectures of L. Prandtl*. Dover, New York.

Tucker, V. A. (1987). Gliding birds: the effect of variable wing span. *Journal of Experimental Biology*, 133(1):33–58.

Tucker, V. A. (1991). The effect of molting on the gliding performance of a Harris' hawk (*Parabuteo unicinctus*). *The Auk*, 108(1):108–113.

Tucker, V. A. and Heine, C. (1990). Aerodynamics of gliding flight in a Harris' hawk, *Parabuteo unicinctus*. *Journal of Experimental Biology*, 149(1):469–489.

Tucker, V. A. and Parrott, G. C. (1970). Aerodynamics of gliding flight in a falcon and other birds. *Journal of Experimental Biology*, 52(2):345–367.

Usherwood, J. R., Cheney, J. A., Song, J., Windsor, S. P., Stevenson, J. P., Dierksheide, U., Nila, A., and Bomphrey, R. J. (2020). High aerodynamic lift from the tail reduces drag in gliding raptors. *Journal of Experimental Biology*, 223(3).

Wainwright, P. C., Alfaro, M. E., Bolnick, D. I., and Hulsey, C. D. (2005). Many-to-one mapping of form to function: a general principle in organismal design? *Integrative and Comparative Biology*, 45(2):256–262.

Waldrop, L. D., He, Y., and Khatri, S. (2018). What can computational modeling tell us about the diversity of odor-capture structures in the Pancrustacea? *Journal of Chemical Ecology*, 44(12):1084–1100.

Weimerskirch, H., Chastel, O., Barbraud, C., and Tostain, O. (2003). Frigatebirds ride high on thermals. *Nature*, 421(6921):333–334.

Weimerskirch, H., Salamolard, M., Sarrazin, F., and Jouventin, P. (1993). Foraging strategy of wandering albatrosses through the breeding season: a study using satellite telemetry. *The Auk*, 110(2):325–342.

Winslow, J., Otsuka, H., Govindarajan, B., and Chopra, I. (2018). Basic understanding of airfoil characteristics at low Reynolds numbers (10 4–10 5). *Journal of Aircraft*, 55(3):1050–1061.

Withers, P. C. (1981). An aerodynamic analysis of bird wings as fixed aerofoils. *Journal of Experimental Biology*, 90(1):143–162.

Xiu, D. and Karniadakis, G. E. (2003). Modeling uncertainty in flow simulations via generalized polynomial chaos. *Journal of Computational Physics*, 187(1):137–167.

Xiu, D., Lucor, D., Su, C.-H., and Karniadakis, G. E. (2003). Performance evaluation of generalized polynomial chaos. In *International Conference on Computational Science*, pages 346–354. Springer.

Yi, M., LIU, Y., JIN, J., and Qian, C. (2010). Analysis of the aerodynamic character of bionic wingspan on the basis of frigate wing structure. *Advances in Natural Science*, 3(2):330–337.

Young, J., Walker, S. M., Bomphrey, R. J., Taylor, G. K., and Thomas, A. L. (2009). Details of insect wing design and deformation enhance aerodynamic function and flight efficiency. *Science*, 325(5947):1549–1552.

Zheng, L., Hedrick, T. L., and Mittal, R. (2013). Time-varying wing-twist improves aerodynamic efficiency of forward flight in butterflies. *PloS One*, 8(1).

5 Tables

	Max C_L/C_D	α_{I}	C_L slope	C_L y_{int}	C_L at $V_{z,\min}$	$V_{z,\min}$ (constant mass)	$V_{z,\min}$ (constant wing loading)
AR	0.44	0.28	0.99	0.13	0.13	0.69	0.76
Q	0.47	0.59	3.3×10^{-3}	0.84	0.84	0.15	0.18
Re	0.054	2.7×10^{-3}	3.0×10^{-6}	1.3×10^{-6}	2.7×10^{-4}	2.1×10^{-3}	0.027
AR & Q	0.022	0.026	4.2×10^{-4}	0.025	0.021	0.056	0.032
AR & Re	8.2×10^{-3}	1.9×10^{-4}	6.6×10^{-7}	4.0×10^{-8}	2.8×10^{-8}	0.012	8.2×10^{-4}
Q & Re	7.6×10^{-3}	0.098	2.1×10^{-6}	8.5×10^{-7}	8.9×10^{-3}	0.093	4.3×10^{-3}
All parameters	1.7×10^{-6}	6.0×10^{-4}	4.7×10^{-8}	1.9×10^{-10}	4.2×10^{-4}	7.1×10^{-8}	8.0×10^{-5}

Table 1: Sobol indices calculated for output performance variables for each parameter and their interactions.

Figures

Figure 1: Birds from each group: pelagic soarers (top left), land soarers (top right), songbirds (bottom row). From top left clockwise: great frigatebird, *Fregata minor* (inset: great frigatebird in flight); Galápagos hawk, *Buteo galapagoensis* (inset: Galápagos hawk in flight); Genovesa ground finch, *Geospiza acutirostris*; Galápagos mockingbird, *Mimus parvulus bauri*; medium ground finch, *Geospiza fortis*.

Figure 2: Gliding flight in birds. Top: free-body diagram of a gliding bird, orientation of D (drag force), L (lift force), and mg (bird's weight). The glide angle is indicated by γ. Middle: diagram of the breakdown of flight speed (V) with its components: horizontal speed (V_x) and sinking speed (V_z). Bottom: cross-section of the wing showing camber, angle of attack (α), and the chordwise camber center line (Q_{line}).

Figure 3: Model of bird aspect ratio (AR) of 5.97 and chordwise camber (Q) of 0.100. A: plan-area view of model bird showing wing length (W), one-half of plan area (S) highlighted in gray, and wing sections measure 1: 0.059 m, 2: 0.140 m, 3: 0.139 m, 4: 0.129 m, 5: 0.099 m, and 6: 0.034 m. $\overline{C} = 0.1$ m. B: cross section of wing taken at a numbered line 3 in A. Wing maximum height t and chord C labeled used to calculate Q. C: Model in XFLR5 at angle of attack $\alpha = 5°$ and Reynolds number $Re = 72,700$ showing calculated streamlines from ring VLM (purple lines) and lift generated by each wing section (green lines). D: Polar curves for lift coefficient (C_L) to drag coefficient (C_D) for a variety of speeds in m s^{-1}. E: Polar curves for C_L/C_D versus α for a variety of speeds (V) in m s^{-1}. Max C_L/C_D and α_{I} were found at the peak of each curve, shown here for $V = 10.9$ m s^{-1}. F: Raw simulation data of maximum lift-to-drag ratio (max C_L/C_D; colored points) against three parameters. G: Surrogate function of max C_L/C_D (colors) produced from raw data in F. In both F and G, color scale for max C_L/C_D is identical to Fig. 4 left. Note: the model's body is disregarded in aerodynamic analysis.

Figure 4: Surrogate functions and Sobol indices for maximum lift-to-drag ratio (C_L/C_D, left column) and lift coefficient (C_L) at minimum sinking speed ($V_{z,\min}$), right column. Top: three-dimensional surrogate function plot with three parameters as the three axes (aspect ratio AR, camber Q, and Reynolds number $Re \times 1000$) and color plotted as the output value. Grey rectangle indicates slice taken at $Re = 105,000$ and presented in the middle column. Color scales in each column consistent with top and middle figures. Bottom: Sobol indices for each parameter and interaction between parameters.

Figure 5: Two-dimensional surrogate functions and Sobol indices for minimum sinking speed ($V_{z,\min}$). Left column: $V_{z,\min}$ with constant wing loading of 7.5 kg m^{-2}. Right column: $V_{z,\min}$ with constant bird mass of 0.90 kg. Top: slices of the three-dimensional function camber (Q) versus aspect ratio (AR) taken at Reynolds number (Re) of 105,000 (similar to middle row of Fig. 4). Scales are in m s^{-1}. Bottom: Sobol indices for outputs for each parameter and their interactions.

Figure 6: Two-dimensional surrogate functions and Sobol indices for ideal angle of attack (α_{I}). Top: slice of the three-dimensional function camber (Q) versus aspect ratio (AR) taken at Reynolds number (Re) of 105,000, scale in degrees. Black line on left plot indicates isocontour where $\alpha_{\mathrm{I}} = 0$. Bottom: Sobol indices for each parameter and their interactions.

Birds from each group: pelagic soarers (top left), land soarers (top right), songbirds (bottom row). From top left clockwise: great frigatebird, *Fregata minor* (inset: great frigatebird in flight); Galápagos hawk, *Buteo galapagoensis* (inset: Galápagos hawk in flight); Genovesa ground finch, *Geospiza acutirostris*; Galápagos mockingbird, *Mimus parvulus bauri*; medium ground finch, *Geospiza fortis*.

96x89mm (300 x 300 DPI)

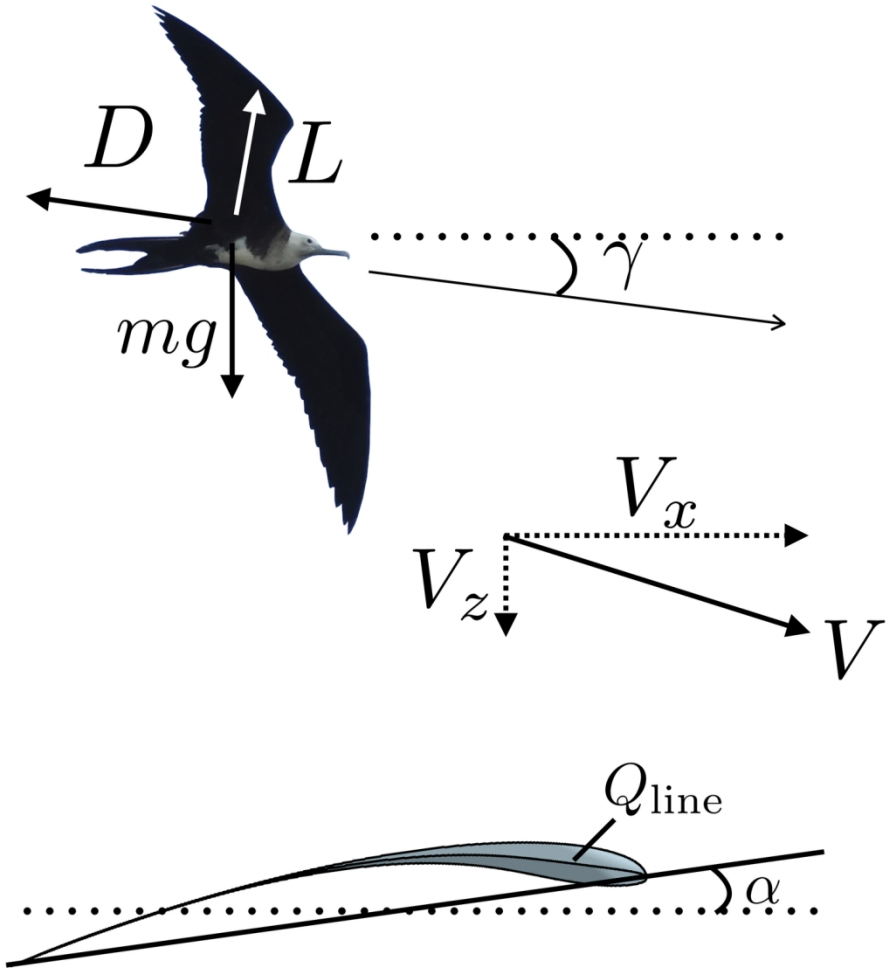

Gliding flight in birds. Top: free-body diagram of a gliding bird, orientation of *D* (drag force), *L* (lift force), and *mg* (bird's weight). The glide angle is indicated by γ. Middle: diagram of the breakdown of flight speed (*V*) with its components: horizontal speed (V_x) and sinking speed (V_z). Bottom: cross-section of the wing showing camber, angle of attack (α), and the chordwise camber center line (Q_{line}).

141x149mm (300 x 300 DPI)

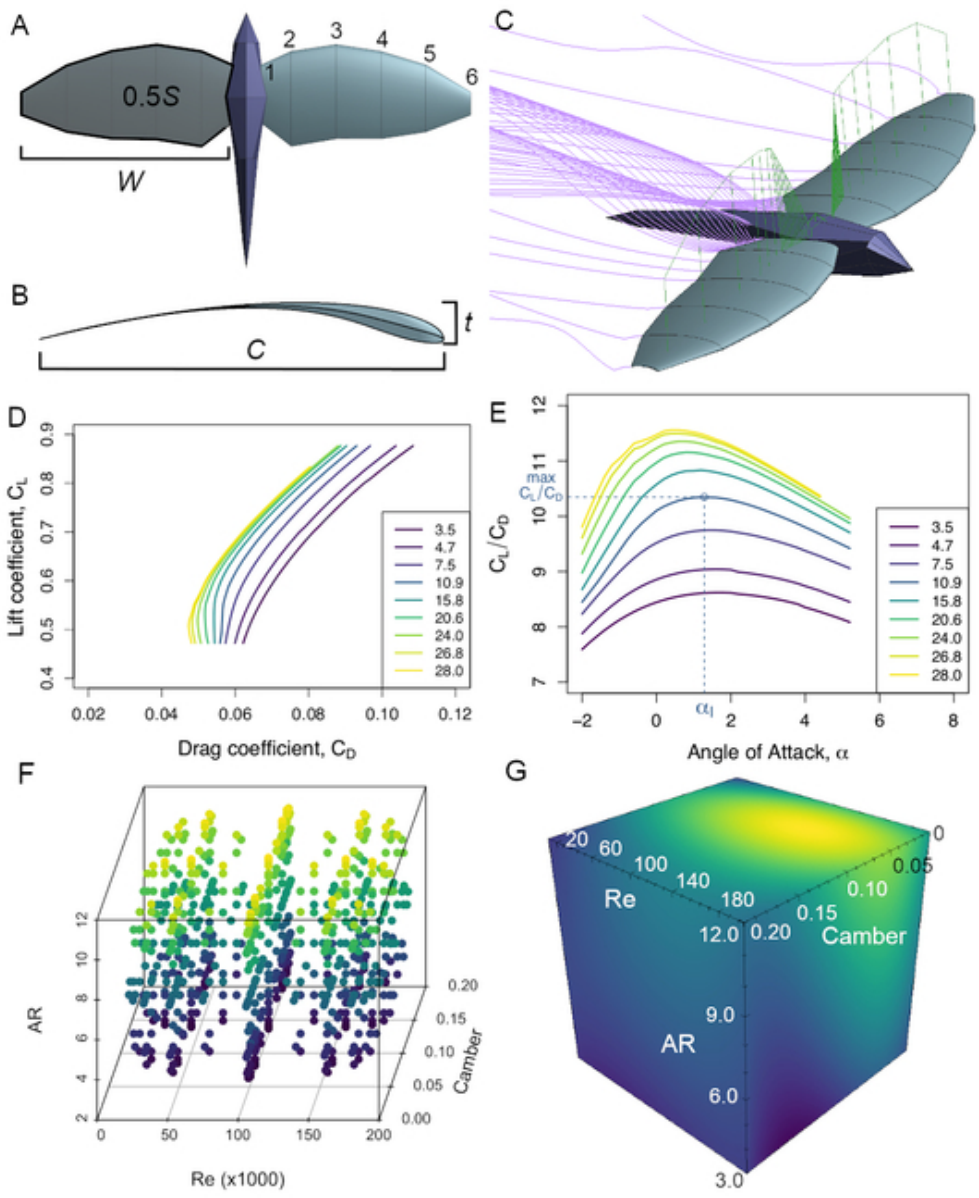

Model of bird aspect ratio (*AR*) of 5.97 and chordwise camber (*Q*) of 0.100. A: plan-area view of model bird showing wing length (*W*), one-half of plan area (*S*) highlighted in gray, and wing sections measure 1: 0.059 m, 2: 0.140 m, 3: 0.139 m, 4: 0.129 m, 5: 0.099 m, and 6: 0.034 m. *C* = 0.1 m. B: cross section of wing taken at a numbered line 3 in A. Wing maximum height *t* and chord *C* labeled used to calculate *Q*. C: Model in XFLR5 at angle of attack α = 5° and Reynolds number *Re* = 72,700 showing calculated streamlines from ring VLM (purple lines) and lift generated by each wing section (green lines). D: Polar curves for lift coefficient (C_L) to drag coefficient (C_D) for a variety of speeds in m s^{-1}. E: Polar curves for C_L/C_D versus α for a variety of speeds (V) in m s−1. Max CL/CD and α_I were found at the peak of each curve, shown here for V = 10.9 m s^{-1}. F: Raw simulation data of maximum lift-to-drag ratio (max C_L/C_D; colored points) against three parameters. G: Surrogate function of max C_L/C_D (colors) produced from raw data in F. In both F and G, color scale for max C_L/C_D is identical to Fig. 4 left. Note: the model's body is disregarded in aerodynamic analysis.

45x54mm (300 x 300 DPI)

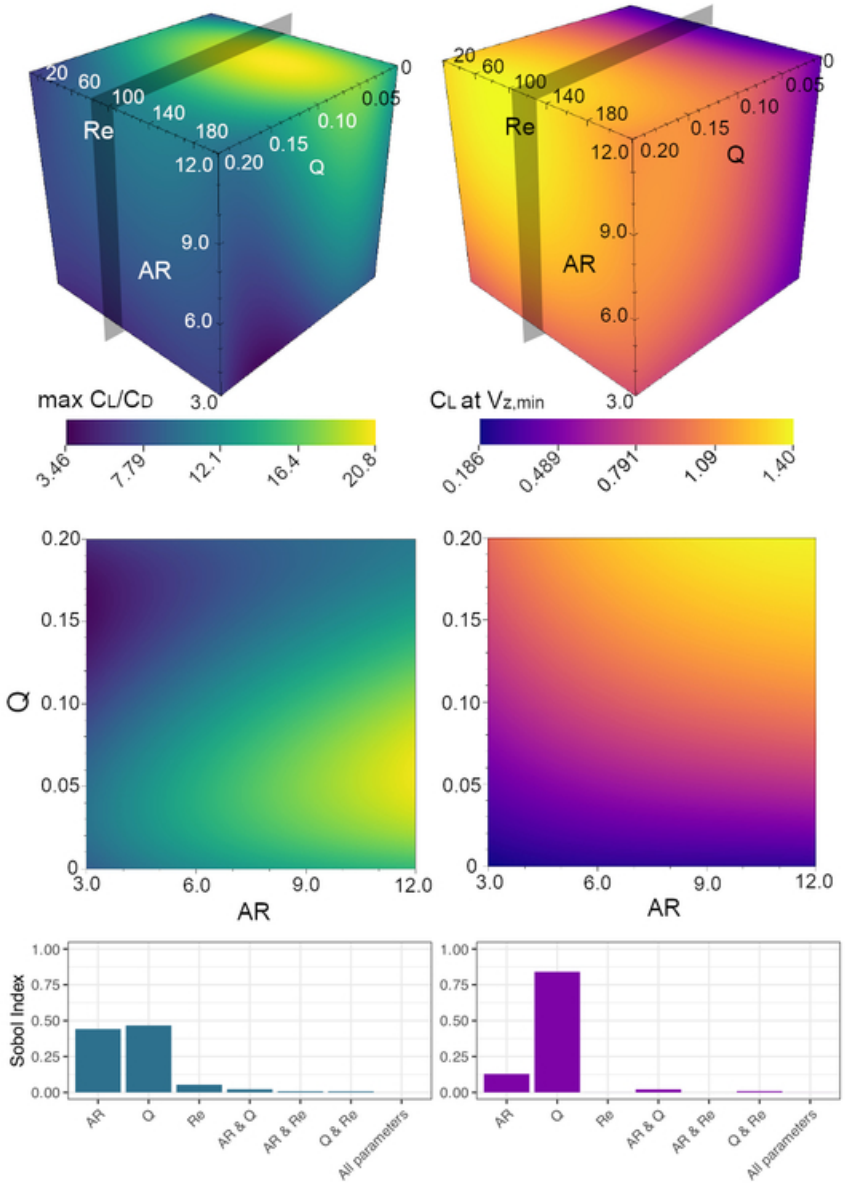

Surrogate functions and Sobol indices for maximum lift-to-drag ratio (C_L/C_D, left column) and lift coefficient (C_L) at minimum sinking speed ($V_{z,min}$), right column. Top: three-dimensional surrogate function plot with three parameters as the three axes (aspect ratio *AR*, camber *Q*, and Reynolds number *Re* × 1000) and color plotted as the output value. Grey rectangle indicates slice taken at *Re* = 105,000 and presented in the middle column. Color scales in each column consistent with top and middle figures. Bottom: Sobol indices for each parameter and interaction between parameters.

45x63mm (300 x 300 DPI)

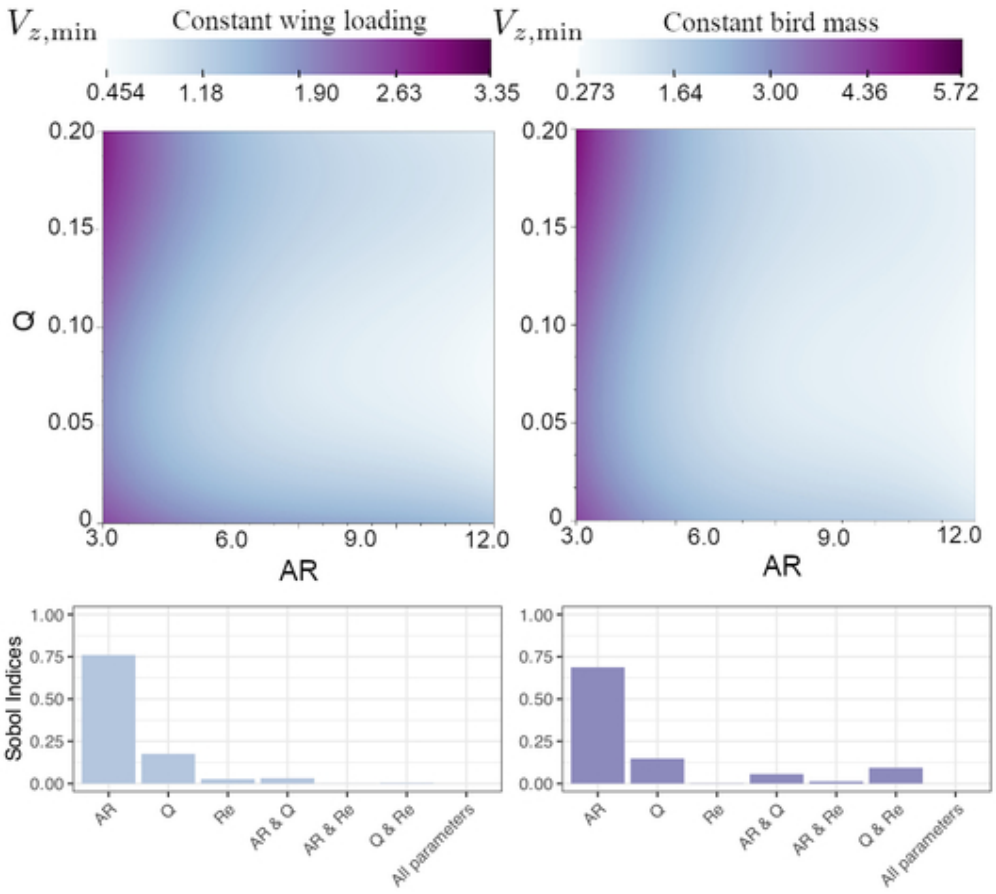

Two-dimensional surrogate functions and Sobol indices for minimum sinking speed ($V_{z,min}$). Left column: $V_{z,min}$ with constant wing loading of 7.5 kg m^{-2}. Right column: $V_{z,min}$ with constant bird mass of 0.90 kg. Top: slices of the three-dimensional function camber (Q) versus aspect ratio (AR) taken at Reynolds number (Re) of 105,000 (similar to middle row of Fig. 4). Scales are in m s^{-1}. Bottom: Sobol indices for outputs for each parameter and their interactions.

44x40mm (300 x 300 DPI)

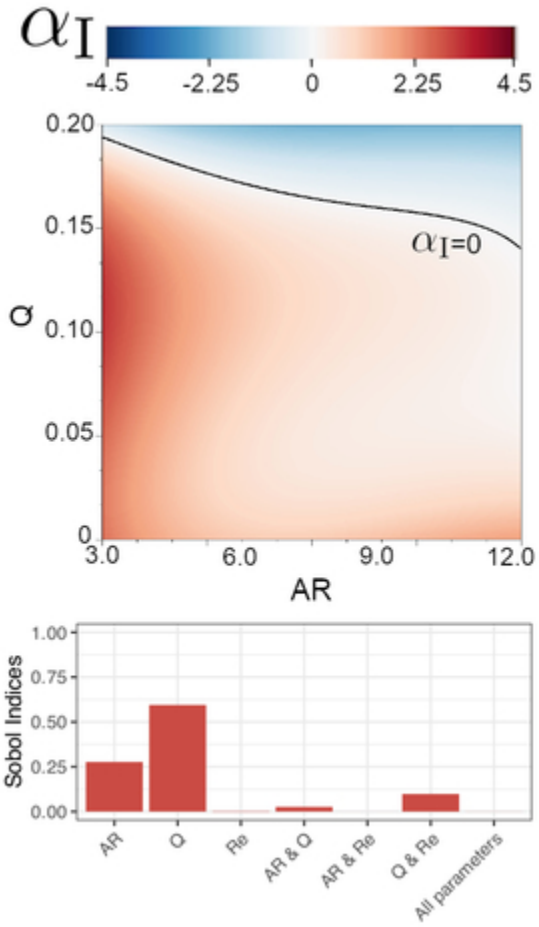

Two-dimensional surrogate functions and Sobol indices for ideal angle of attack (α_I). Top: slice of the three-dimensional function camber (*Q*) versus aspect ratio (*AR*) taken at Reynolds number (*Re*) of 105,000, scale in degrees. Black line on left plot indicates isocontour where $\alpha_I = 0$. Bottom: Sobol indices for each parameter and their interactions.

23x40mm (300 x 300 DPI)